



Enhanced oxidation resistance in refractory niobium by surface Ti⁺/Si⁺ implantation

Ping-Jiong Yang, Wei-Zhong Han*

Center for Advancing Materials Performance from the Nanoscale, State Key Laboratory for Mechanical Behavior of Materials, Xi'an Jiaotong University, Xi'an 710049, PR China



ARTICLE INFO

Keywords:

Niobium
Oxidation
Ion implantation
Oxygen gettering effect

ABSTRACT

Massive oxides growth during service inevitably degrade the performance of oxygen sensitive refractory metals. Here, we propose to improve the oxidation resistance of niobium by surface implantation of Ti⁺ and Si⁺. After oxidation, oxides in niobium not only form at topmost surface, but also massively grow along {100} planes. In contrast, oxides at top surface can be efficiently suppressed by implantation of Ti⁺ and Si⁺. No detectable oxides were formed after Si⁺ implantation, while some laminated oxides bundles can still be detected in Ti⁺ implanted sample, indicating Si⁺ has a stronger effect in improving oxidation resistance.

1. Introduction

Oxidation has long been an impassable issue for the production and service of metallic materials [1–3], especially for the components served in harsh environments like refractory metals [4–6]. Among them, niobium is recognized as essential high temperature structure components in rockets or aircrafts, due to its superior high temperature strength, creep resistance and relative low density compared with other refractory metals [7,8]. However, as oxygen has a high affinity to niobium, oxygen solutes can quickly diffuse into niobium matrix and form oxides [9,10]. Owing to the large surface expansion caused by the formation of oxides, cracks easily nucleate and propagate over the whole surface area [11,12]. In this way, niobium based structure components often lose its ductility and collapse under unpredictable low stress with limited lifetime.

To overcome the oxidation induced failure, typical anti-oxidation strategies like alloying [13,14] and surface barrier coating [15,16] have been put out to suppress high temperature oxidation. Reactive elements such as Si, Al, Cr, Ti, Hf, and Y etc., all of which exhibit a higher affinity to oxygen than niobium matrix [17], are frequently utilized as alloying elements in fabrication of oxidation resistant niobium alloys [13–19]. Specially, Si, Al and Cr are believed to suppress oxidation by promoting the formation of dense and protective oxide film at oxidized surface, which block the deep diffusion of external oxygen [16,20]. In contrast, Ti, Hf, and Y are typical alloying elements used to trap oxygen because of their stronger interaction with oxygen than Nb, thus lowering the diffusivity of oxygen in matrix [19,20]. Typically, most anti-oxidation

design is performed in a complex alloying system with the characteristics of multiple alloying constituents and/or high alloying concentration, which usually play their role with distinct degradation of melting points, ductility or other physical properties [15]. Therefore, how to precisely control the surface inner structure in niobium to tune the oxidation resistance without changing the properties of original alloy is still remain elusive.

Based on the knowledge of the reactive elements addition on oxidation behavior, it is possible to tune oxidation properties of niobium alloy by surface introducing of selected elements. While researches on the effect of single element addition on anti-oxidation behavior mainly focus on the oxidation kinetics [13,21], an integrated understanding based on inner microstructure evolution is rarely reported. In this study, we employ ion implantation to introduce the anti-oxidation elements on the surface of niobium to evaluate their effect on the oxidation behavior. Ion implantation has been proved to be an efficient research tool to evaluate alloying effect on oxidation behavior of metallic metals [21–24]. Ti and Si were selected as model elements according to previous studies [16,19,20] and introduced into the surface region of high purity niobium by ion implantation. With the aid of advanced sample lifting technique, the surface oxidation structures were systematically examined and analyzed, and the effectiveness of Ti and Si on oxidation resistance of niobium is discussed.

2. Materials and methods

High purity niobium (99.99 at.%) slices with the size of

* Corresponding author.

E-mail address: wzhanxjtu@mail.xjtu.edu.cn (W.-Z. Han).

<https://doi.org/10.1016/j.corsci.2019.108297>

Received 13 June 2019; Received in revised form 9 September 2019; Accepted 17 October 2019

Available online 21 October 2019

0010-938X/ © 2019 Elsevier Ltd. All rights reserved.

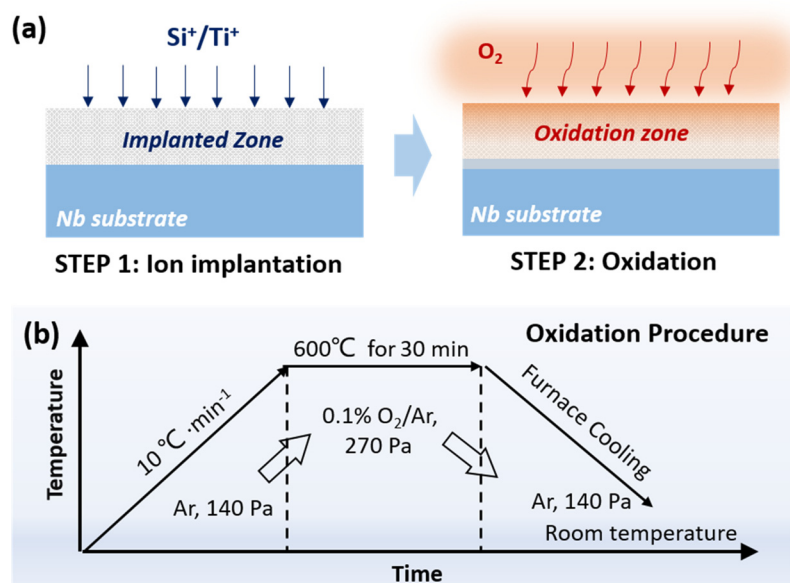


Fig. 1. Schematic illustration of ion implantation and subsequent surface oxidation process of high purity Nb. (a) Schematic illustration of ion implantation and subsequent surface oxidation process. (b) Schedule of heat treatment and oxidation experiments.

1 cm × 1 cm × 2 mm were selected as our model sample. Recrystallization annealing was performed at 1000 °C for 1 h with the vacuum of 10⁻⁴ Pa. Afterwards, all the Nb slices were carefully grinded via 320#, 500#, 800#, 1200# and 2400# abrasive paper to get a flat surface, and then polished with minor diamond polishing fluid with ~ 0.5 μm in particle size added on a polishing machine. To eliminate the surface stress or deformation layer introduced during the polishing process, the polished surfaces were etched slightly using a cotton with a mixed acid of 10% HF, 10% HNO₃ and 80% water (in volume percentage). Note that each sample was quickly washed after etching to get rid of the remaining acid on the surface. As illustrated in Fig. 1(a), the following processing can be divided into two steps, ion implantation and oxidation. More details are shown below.

First, Si⁺ and Ti⁺ ions were implanted into Nb slices at room temperature with the accelerate voltage of 400 kV to a fluence of 3 × 10¹⁶ ions cm⁻² for Si⁺ and 2 × 10¹⁶ ions cm⁻² for Ti⁺, respectively. Thus, the corresponding flux rates are 1 × 10¹³ ions cm⁻² s⁻¹ for Si⁺ and 5.55 × 10¹² ions cm⁻² s⁻¹ for Ti⁺. The sample with Si⁺ implantation is named as ‘Nb-Si’, while the sample with Ti⁺ implantation is named as ‘Nb-Ti’ in the following section. As shown in Fig. 2(a) and (b), the corresponding ion concentration and damage along depth was estimated with SRIM (the Stopping and Range of Ions in Matter) simulation using full cascade damage mode with an average displacement energy of 35 eV [25]. Both of the implantation depth are no more than 450 nm and the maximum concentration of implanted ions are less than 3 at.%. In addition, ion implantation induced damage is extremely high and the peak damage is approaching ~ 80 dpa for Nb-Si and ~ 60 dpa for Nb-Ti, respectively. The XRD patterns after implantation (shown in Fig. 2(c)) shows no distinct change in microstructures compared with original high purity Nb, indicating no obvious precipitates/oxides forms during ion implantation. Therefore, the implanted ions should exist as solutes after ion implantation in Nb matrix. To further analyze the effect of ion implantation on niobium, the hardness variation before and after ion implantation was measured by nanoindentation (TI 950 Triboindenter). The maximum indentation force was set as 6000 μN and more than six repeated tests were performed for each sample. The resultant load-depth curve achieved in indentation test shows that the maximum indentation depth is ~ 302 nm for Nb, ~ 298 nm for Nb-Ti and ~ 256 nm for Nb-Si, as shown in Fig. 2(d). Therefore, the maximum indentation depth of all the samples falls into the region of the ion implanted zone. The measured hardness is an average value for the ion implanted

region.

Afterwards, all the samples (Nb, Nb-Si and Nb-Ti) were oxidized at the same time in a tube furnace. The procedures of oxidation experiments is shown in Fig. 1(b). Considering the limited implantation depth and ion concentration, the oxidation conditions was set as 600 °C for 30 min within the controlled atmosphere of 0.1% O₂(volume percent) in high-purity argon. Finally, the oxidation surface was analyzed by scanning electron microscope (SEM). The cross-sectional sample was made by typical sample lifting technique inside focus ion beam (FIB) system. Platinum (Pt) was utilized to protect oxidized surface from ion damage during FIB fabrication process. The oxidation structures characterization was conducted inside a transmission electron microscope (TEM, JEOL-2100 F).

3. Results

3.1. Surface morphology after oxidation

The oxidized surface was firstly examined under SEM, as shown in Fig. 3. For Nb, irregular local bulges with the size of several micrometers can be seen across the whole oxidized surface (Fig. 3(a)). In contrast, the surface morphology of oxidized Nb-Ti appears to be different. As can be seen in Fig. 3(b), distinct surface wrinkles with the length of hundreds of micrometers are formed. Particularly, the local wrinkles are parallel to each other with the spacing of ~ 10 μm (Fig. 3(c)). No distinct irregular surface bulge structures were found in Nb-Ti sample. While for Nb-Si, the oxidized surface is quite smooth with only seldom tiny local bulges formed, as shown in Fig. 3(d). The distinct oxidation morphology for Nb with and without ion implantation suggests that the oxidation resistance can be tailored by ion implantation of selected oxygen affinity elements.

3.2. Cross-section microstructures of oxidized Nb

For a clear understanding of the different oxidation morphologies among Nb, Nb-Ti and Nb-Si, the cross-sections microstructure of the top surface were further analyzed in detail. For Nb, mainly two types of oxides have been formed during oxidation according to the contrast difference under SEM, surface oxides at topmost surface and lamella oxides uniformly distributed inside Nb matrix at subsurface, as shown in Fig. 4(a). In addition, distinct inner crack can be observed inside the

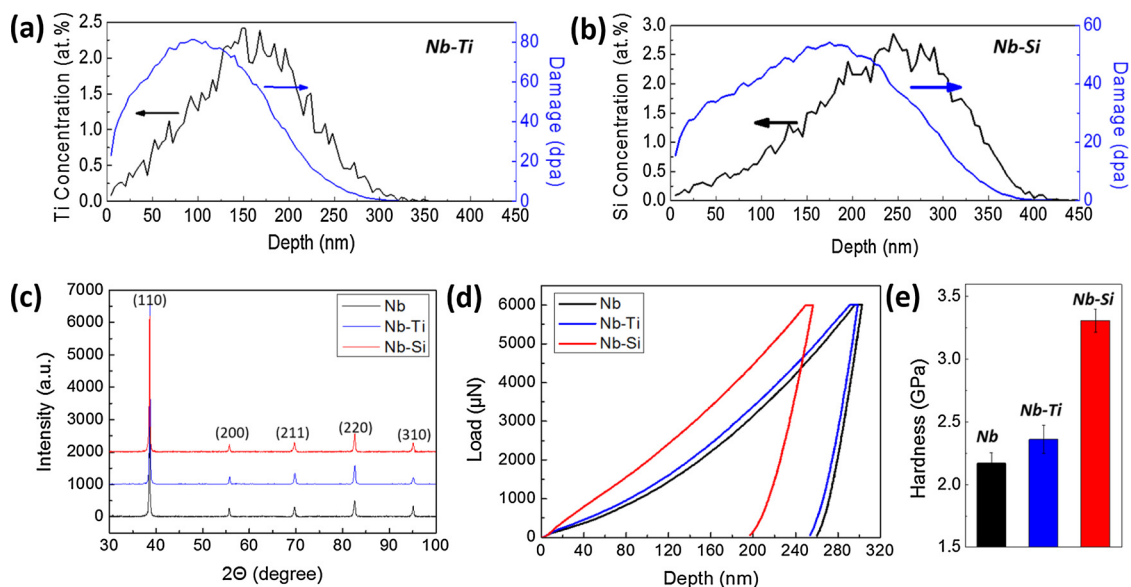


Fig. 2. Ion concentration, surface structure and hardness after Si^+ and Ti^+ implantation in Nb. (a) The Ti concentration and damage distribution in Ti^+ implanted Nb according to SRIM simulation. (b) The Si concentration and damage distribution in Si^+ implanted Nb according to SRIM simulation. (c) The XRD patterns of Nb before and after ion implantation. (d) Representative load-depth curve formed during indentation test before and after ion implantation. (e) Hardness of Nb before and after ion implantation.

surface oxides layer. Further TEM characterization reveals that the thickness of surface oxides layer is $\sim 0.6 \mu\text{m}$, ignoring the existence of the cracks inside (Fig. 4(b)). The thickness of the lamella oxides is about 150 nm, which appears to be uneven, as marked in Fig. 4(c). It is worth noting that the lamella oxides originates from the surface oxides layer, as shown in Fig. 4(c). The corresponding selected area diffraction pattern displayed that the surface oxide and lamella oxide share the same crystal structure. The typical orientation relationship between lamella oxide and niobium matrix is shown in Fig. 4(d). The niobium oxides here is body-centered tetragonal $\alpha\text{-Nb}_2\text{O}_5$, normally seen under a similar oxidation temperature [26]. According to Fig. 4(d), the (200)

planes of Nb matrix are parallel to the (010) planes of $\alpha\text{-Nb}_2\text{O}_5$, indicating that lamella $\alpha\text{-Nb}_2\text{O}_5$ is prone to nucleate and grow along (200) planes of Nb matrix once the oxygen content is above its solubility.

3.3. Cross-section microstructures of Nb-Ti after oxidation

In Nb-Ti, as distinct surface wrinkles can readily take shape during oxidation, cross-section microstructure analysis was also performed, as shown in Fig. 5. After oxidation, the surface of Nb-Ti sample is rather flat, as marked by the white dashed lines in Fig. 5(a). No surface oxides

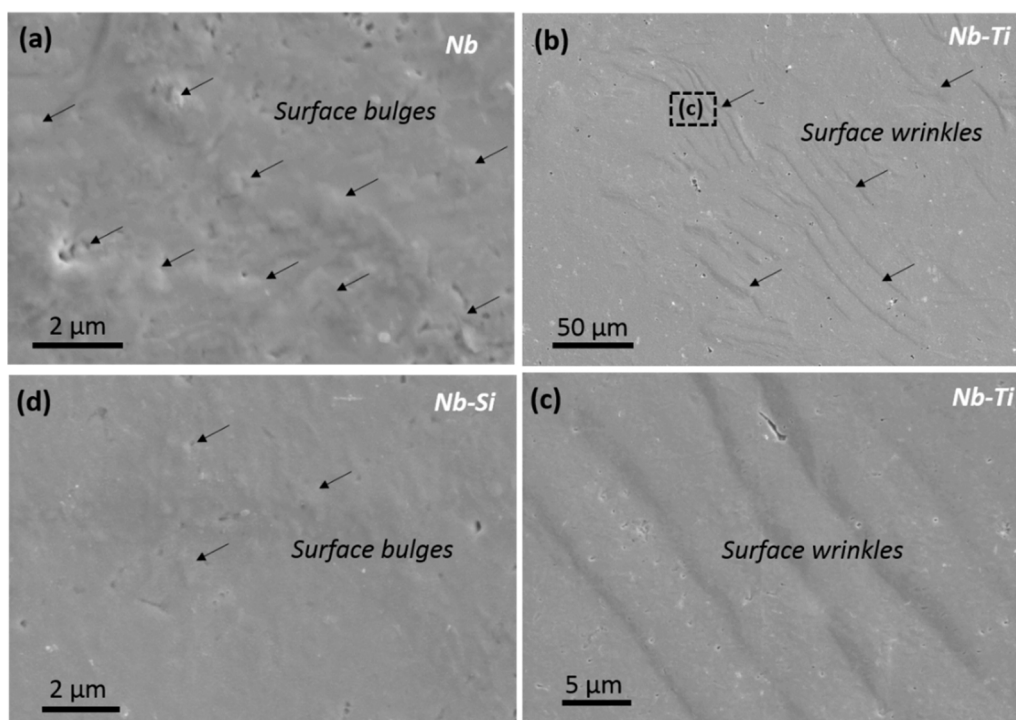


Fig. 3. SEM images of surface morphology of (a) Nb, (b–c) Nb with Ti ion implantation and (d) Nb with Si ion implantation after oxidation experiment.

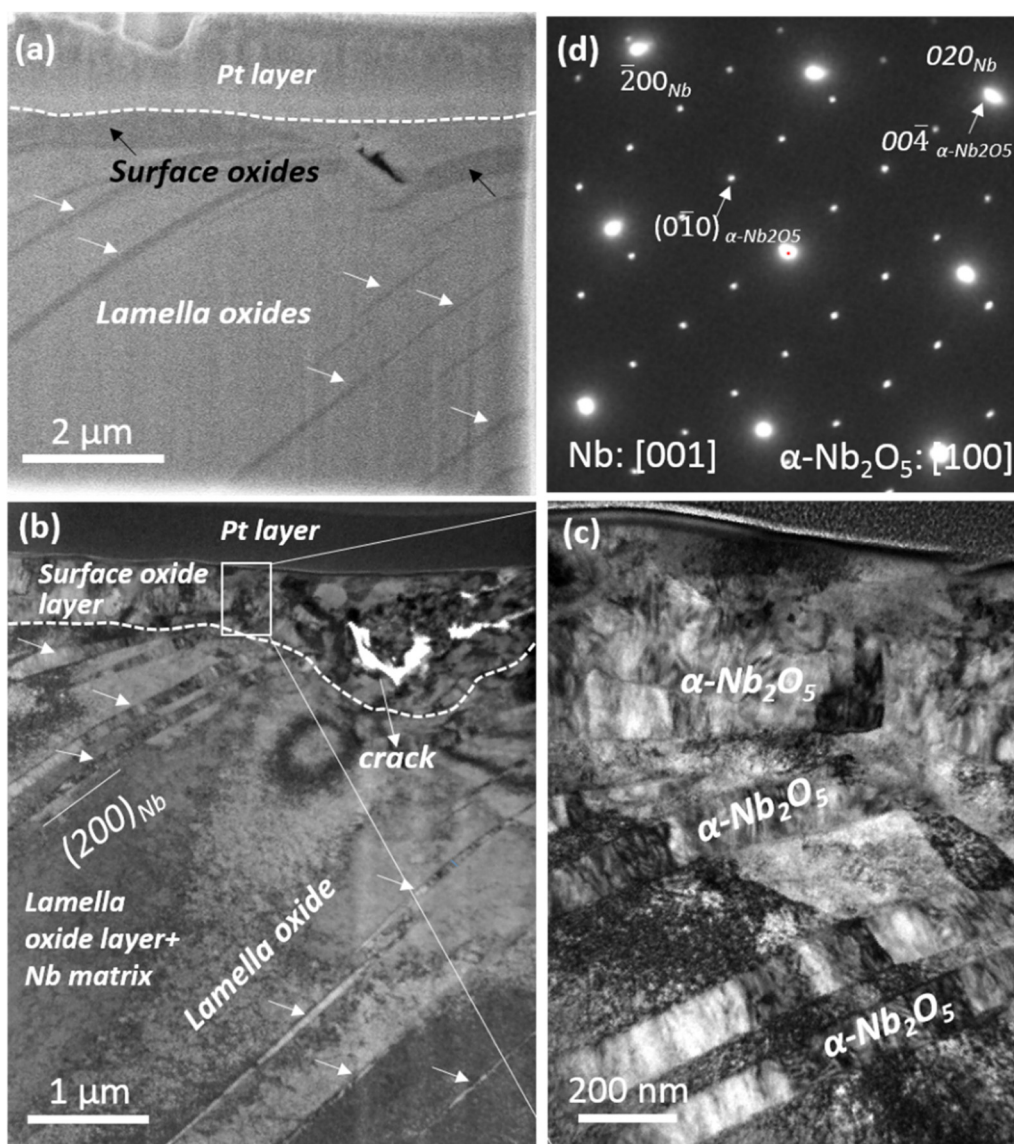


Fig. 4. Cross-section image of the microstructures in oxidized pure Nb. (a) A low magnified SEM image of the cross-section of oxidized pure Nb. (b) A low magnified bright field TEM image of the cross-section of the microstructures formed in oxidized pure Nb. The boundary between surface oxide layer and Nb matrix are labeled by the white dashed line. (c) A high magnified TEM image of the oxide layer marked by white box in (b). (d) The selected area diffraction pattern acquired at the interface of Nb matrix and lamella $\alpha\text{-Nb}_2\text{O}_5$ oxide.

can be observed at topmost surface, which is different from the observation in Fig. 4 for Nb. However, two bundles of laminated structure with the thickness of $\sim 1 \mu\text{m}$ formed inside Nb matrix at the subsurface, which is different from the dispersed laminated oxides with high density inside the matrix of oxidized niobium. Further TEM characterization demonstrates that there is no detectable niobium oxides at topmost surface as well, as shown in Figs. 5 (c) and (d). Only a thin layer of ultrafine grains within the depth of $\sim 1 \mu\text{m}$ at topmost surface region was observed. This is caused by rearrangement of radiation defects during ion implantation [27,28], on the base of extremely large radiation damage introduced by ion implantation, as shown in Figs. 2(a). The ion implantation induced ultrafine-grain in the top surface region also contributes to the surface hardening (Fig. 2(e)). As for the lamella oxide bundles, the thickness of single lamella is comparable to that formed in oxidized niobium. Meanwhile, these oxides are also body-centered tetragonal $\alpha\text{-Nb}_2\text{O}_5$ type oxide with a similar orientation as the oxides in Nb, as demonstrated in Figs. 5 (e) and (f). In brief, Ti^+ implantation can fully suppress the surface oxides formation and regulate the subsurface lamella oxides as bundles during oxidation. While

nearly ~ 2.68 volumn expansion occurs with the formation of $\alpha\text{-Nb}_2\text{O}_5$ [12], the nucleation of lamella oxides bundles at subsurface region will give rise to a distinct wrinkle morphology on the top of the oxidized surface, as shown in Fig. 3(b). Because of the growth of lamella oxides exhibits preferred crystallographic features along the $\{100\}$ planes of niobium matrix, the local wrinkles are seen to be parallel to each other (Fig. 3(d)).

3.4. Cross-section microstructures of Nb-Si after oxidation

For Nb-Si, no distinct oxides morphology can be detected after oxidation processing, as shown in Fig. 6(a). At the topmost surface, a layer of ultrafine grains can also be observed (Fig. 6(b)), similar to that of Nb-Ti in Fig. 5(b), as a result of radiation defects rearrangement during ion implantation with radiation damage around 70 dpa, as shown in Figs. 2(b) [27,28]. The corresponding diffraction pattern reveals that the ultrafine grain region consists of body-centered-cubic niobium with no oxides or precipitates formation (Fig. 6(c)), consistent with the XRD results in Fig. 2(c). While for the subsurface beneath the

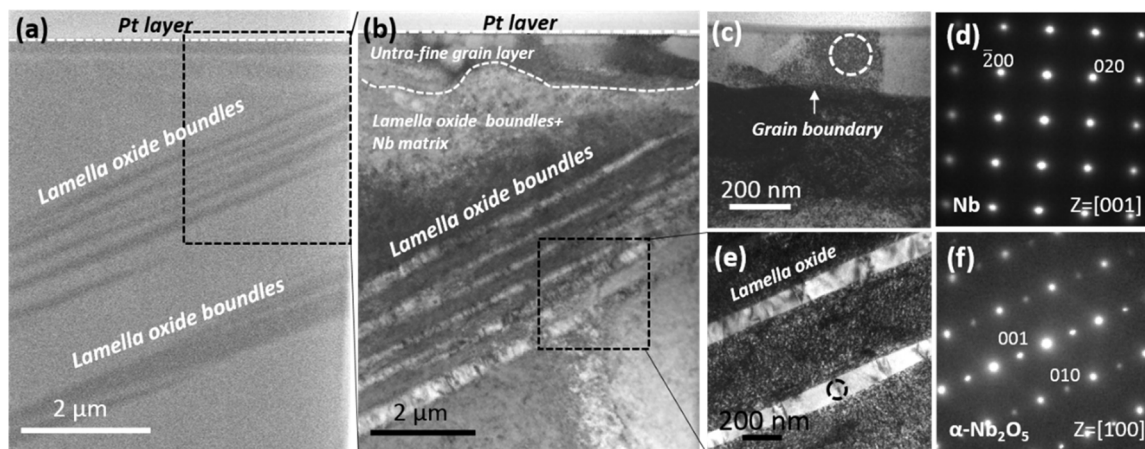


Fig. 5. Cross-section images of microstructures formed in oxidized Nb with Ti ion implantation. (a) A low magnified SEM image showing the cross-section of the microstructures formed in oxidized Nb with Ti ion implantation. (b) An enlarged bright field TEM image of the surface region labeled in the dashed box region in (a). (c) An enlarged bright field TEM image of the ultra-fine grain region at topmost surface in (b). (d) Corresponding diffraction pattern in the dashed circled region in (c). (e) An enlarged bright field TEM image of the lamella oxides in (b). (f) Corresponding selected area diffraction pattern of the dashed circled region in (e).

ultrafine grain layer, slight contrast with lamella morphology can be detected from the bright field image in Fig. 6(d). However, the corresponding diffraction pattern demonstrate that no detectable new phase were formed in this region, which indicates that the formation of oxides were fully suppressed at subsurface in Nb-Si. These observations demonstrate that, Si⁺ implantation can simultaneously suppress surface oxides formation and subsurface lamella oxides growth during oxidation, which has a higher influence in improving the oxidation resistance of niobium than Ti⁺.

4. Discussion

4.1. Oxidation of Nb at 600 °C

As for high temperature oxidation of niobium, with stable and dense amorphous oxide well bonded to niobium matrix, niobium is free of oxidation below 400 °C [12,26]. But with increasing temperature, loose

α -Nb₂O₅ nucleates accompanied by a factor of 2.68 vol expansion, breaking original protective surface oxides and facilitating continuous oxidation [26,29]. Afterwards, oxygen diffuses freely in Nb matrix and accumulate to form oxides when local oxygen concentration exceeds its solubility. Since the diffusion rate of oxygen in Nb is $D = 4.55 \times 10^{-3} \exp(-25900/RT) \text{ cm}^2\text{s}^{-1}$ [10], the maximum diffusion distance L can be estimated using Fick's Law $L = \sqrt{4Dt}$, where $R = 1.987 \text{ cal}\cdot\text{K}^{-1} \text{ mol}^{-1}$, T is the oxidation temperature and t is oxidation duration. As the oxidation was conducted at 600 °C for 30 min in our case, the corresponding diffusion distance is $\sim 33 \mu\text{m}$, far exceeding our detection region with the maximum depth of $\sim 5 \mu\text{m}$. Therefore, it is reasonable to form oxides at the depth of our detection region. In real oxidation process at 600 °C, O₂ is continuously absorbed and decomposed at niobium/atmosphere interface, causing high oxygen concentration at surface region. Therefore, the oxides at topmost surface take the shape rapidly. Meanwhile, due to high diffusion rate of oxygen in niobium mentioned above, massive oxygen quickly diffuse into niobium matrix

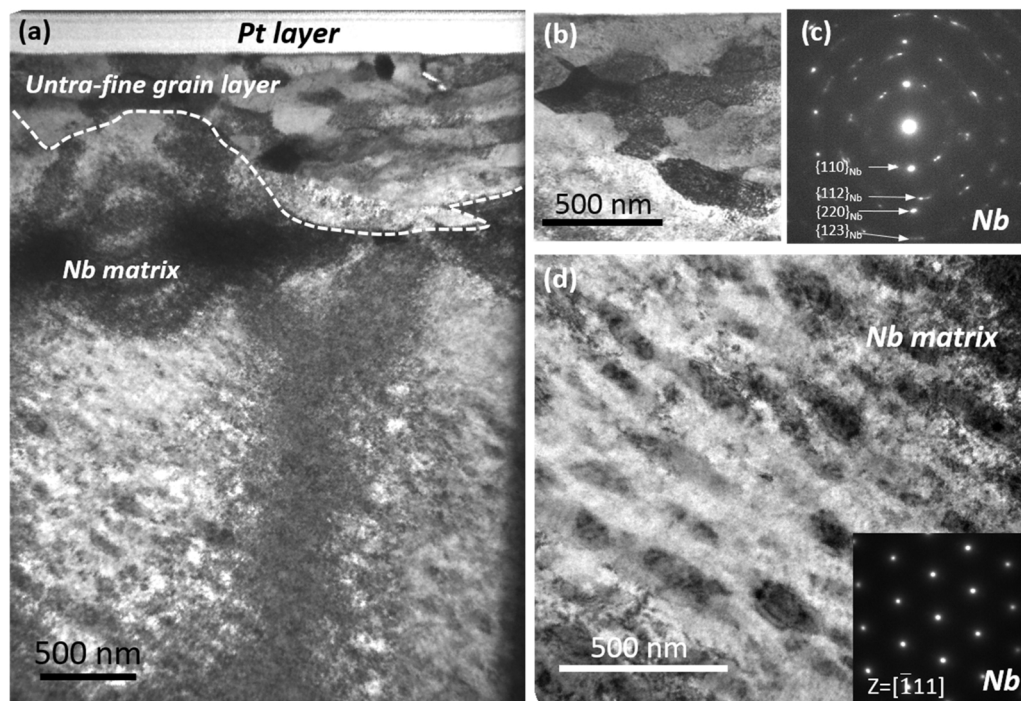


Fig. 6. Cross-section TEM images of microstructures in oxidized Nb with Si ion implantation. (a) A low magnified bright field TEM image showing the cross-section of the oxidized Nb with Si implantation. (b-c) The enlarged bright field TEM image of the top ultra-fine grain region and its corresponding selected area diffraction pattern. (d-e) The enlarged bright field TEM image of niobium matrix and its corresponding diffraction pattern.

and saturate. Similar to the characteristics that premature niobium oxide nucleates along certain crystallographic planes revealed by in situ TEM [30], oxygen at subsurface tends to accumulate and precipitate out along {100} planes of niobium matrix, forming lamella oxides in Fig. 4.

4.2. Suppressed oxides formation at topmost surface after ion implantation

While for Si^+ and Ti^+ implanted samples, the oxides at topmost surface can be suppressed during oxidation, as shown in Figs. 5 and 6. As Ti and Si have a higher affinity with oxygen than Nb matrix, namely lower ΔG° (standard free energy of formation) value than NbO ($\Delta G_{\text{NbO}_2}^{\circ} > \Delta G_{\text{NbO}}^{\circ} > \Delta G_{\text{SiO}_2}^{\circ} > \Delta G_{\text{TiO}_2}^{\circ}$), oxygen will be preferentially picked up by these two reactive elements to form stable SiO_2 and TiO_2 [17]. In this way, the oxygen concentration in niobium matrix is reduced compared with the samples without ion implantation, leading to a delayed oxides nucleation. Meanwhile, ion implantation induced defects like ultrafine grains shall also play a role. Normally, the reduced grain size or increased defect density will exert two-fold effects on oxidation [31], the increased high energy sites for oxygen segregation [20] and enhanced diffusion kinetics for alloying elements [32]. First, for the effect of increased oxygen segregation sites, vast radiation defects or alloying sites shall act as sinks to absorb oxygen solutes and increase the solubility of oxygen in niobium [23], leading to delayed oxides formation. Moreover, via the enhanced diffusion effect for alloying element (here by Ti and Si), the establishment of SiO_2 and TiO_2 is much more rapid and uniform [17,31], quickly altering surface defect structure and hindering the inward diffusion of oxygen. Note that the Ti or Si concentration is no more than 3% even at the peak concentration region in Nb, thus the resultant TiO_2 and SiO_2 concentration after oxidation should be limited with extremely small size, which is out of the detection limit of TEM.

Based on the analysis above, the whole process of the suppressed oxidation at topmost surface of Si^+ and Ti^+ implanted Nb can be summarized as follows (Fig. 7). Ion implantation firstly produces large amounts of irradiation defects in original sample (Figs. 2(a) and (b)), typically ultrafine grains in our case. Once the temperature is elevated for oxidation, the diffusivity of implanted elements is accelerated with the aid of implantation induced grain boundaries (Figs. 5(b) and 6(b)), leading to rapidly aggregation of reactive elements at topmost surface region. When oxygen is decomposed from atmosphere and diffuses into niobium sample, they will be quickly gettering by the aggregated reactive elements and grain boundaries at topmost surface [17,20], hindering the inward diffusion of following oxygen from atmosphere. While the absorbed oxygen at topmost surface tends to be trapped by the reactive elements or grain boundaries, the oxides at topmost surface are completely suppressed (Figs. 5 and 6).

4.3. Different oxidation structure at subsurface between Nb-Ti and Nb-Si

As for subsurface lamella oxides, Nb-Ti and Nb-Si sample exhibit totally different oxidation features. This is caused by different oxidation products for these two samples. As for Nb-Ti, the oxidation products of Ti is loose, which allows continuously absorption of oxygen into surface region [19]. Although the selective oxidation of Ti at topmost surface shall act as oxidation barrier to restrict the inward diffusion of oxygen as a whole, oxygen can still quickly penetrate into niobium subsurface from the position where local Ti concentration is limited or the barrier is loose. In this way, at subsurface region, lamella oxides will still take the shape in the manner of bundles originating from surface, causing wrinkle morphology at oxidized surface (Figs. 3(b) and (c)). For Nb-Si, it is widely recognized that dense and stable SiO_2 tends to nucleate during high temperature oxidation, forming a protective layer at outside surface and resist the entrance of oxygen [16,18]. Therefore, the formation of lamella oxides at subsurface was delayed due to fully restricted entrance of oxygen from atmosphere. While Si concentration at surface region is limited (Fig. 2(b)), it is hard to capture the signal from silica in our experiment. For the factors above, as depicted in Fig. 7, lamella oxides bundles take the shape from the loose location of oxidized surface in Nb-Ti, while no distinct oxides appear in Nb-Si for its dense and protective oxidized surface.

5. Conclusion

To sum up, a new strategy for improved oxidation resistance in niobium was put out by implantation of oxygen sensitive Ti^+ and Si^+ ions. Two types of surface oxidation products are formed in Nb at 600 °C, exactly topmost surface oxides and subsurface dispersed thin lamella oxides, with $\alpha\text{-Nb}_2\text{O}_5$ type structure. In contrast, for Nb implanted by Ti^+ and Si^+ , the topmost surface oxides can be suppressed due to the gettering effect of oxygen solutes by reactive Ti/Si elements and implantation defects. The subsurface lamella oxides in Ti^+ implanted Nb tend to grow as bundles, contributing to the formation of wrinkle morphology at surface. The Si^+ implanted Nb shows no oxides formed at subsurface region, suggesting stronger oxidation resistance than Ti^+ implanted Nb, which is caused by the dense and protective nature of its oxidation products. Our work demonstrates that enhanced oxidation resistance can be achieved in refractory Nb by ion implantation using well-selected reactive elements, which provides new choices to improve the oxidation resistance of niobium and other metallic materials.

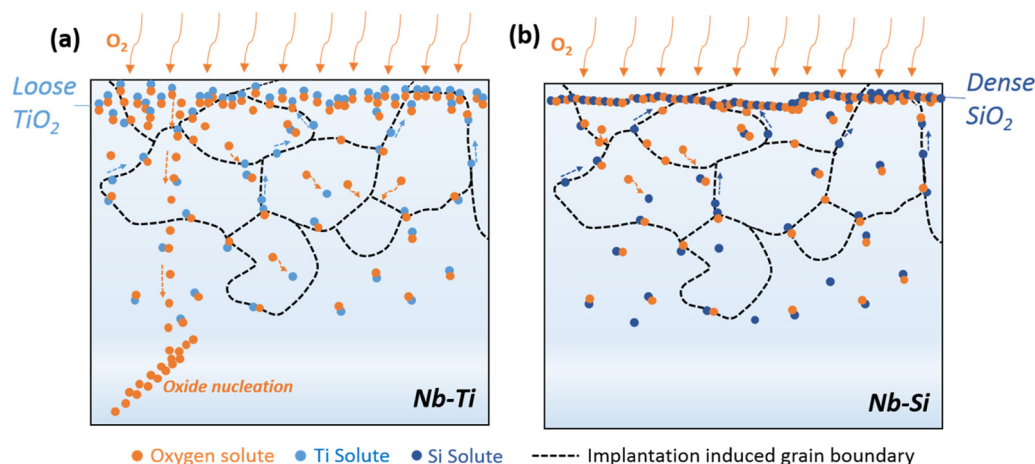


Fig. 7. Schematic illustration for the delayed oxides formation by the gettering effect of reactive elements in (a) Ti^+ implanted Nb and (b) Si^+ implanted Nb.

Declaration of competing interest

The authors declare that there is no conflict of interest regarding the publication of this article.

Acknowledgments

This work was supported by the National Natural Science Foundation of China (Grant Nos. 51971170, 51922082 and 51942104), the National Key Research and Development Program of China (2017YFB0702301), and the 111 Project of China (Grant Number BP2018008).

References

- [1] N.P. Padture, G. Maurice, E.H. Jordan, *Science* 296 (2002) 280–284.
- [2] A. Barrios, S. Gupta, G. Castelluccio, O.N. Pierron, *Nano Lett.* 18 (2018) 2595–2602.
- [3] C.A.L. Leung, S. Marussi, M. Towrie, R.C. Atwood, P.J. Withers, P.D. Lee, *Acta Mater.* 166 (2019) 294–305.
- [4] M.S. El-Genk, J.M. Tournier, *J. Nucl. Phys. Mater. Sci. Radiat. Appl.* 340 (2005) 93–112.
- [5] Y.F. Gu, H. Harada, Y. Ro, *JOM* 56 (2004) 28–33.
- [6] P.J. Yang, Q.J. Li, T. Tsuru, S. Ogata, J.W. Zhang, H.W. Sheng, Z.W. Shan, G. Sha, W.Z. Han, J. Li, E. Ma, *Acta Mater.* 168 (2019) 331–342.
- [7] J.T. Busby, K.J. Leonard, *JOM* 59 (2007) 20–26.
- [8] R. Grill, A. Gnadenberger, *Int. J. Refract. Met. Hard Mater* 24 (2006) 275–282.
- [9] C. Nico, T. Monteiro, M.P.F. Graça, *Prog. Mater. Sci.* 80 (2016) 1–37.
- [10] R.A. Perkins, R.A. Padgett Jr., 25 (1977) 1221–1230.
- [11] C. Valot, D. Ciosmak, M. Lallemand, *Oxid. Met.* 41 (1994) 235–250.
- [12] J. Halbritter, *Appl. Phys. A* 43 (1987) 1–28.
- [13] R. Smith, *J. Less Common Met.* 2 (1960) 191–206.
- [14] J. Zheng, X. Hou, X. Wang, Y. Meng, Zheng X, L. Zheng, *Int. J. Refract. Met. Hard Mater* 54 (2016) 322–329.
- [15] R.A. Perkins, G.H. Meier, *JOM* 42 (1990) 17–21.
- [16] B. Vishwanadh, R.H. Naina, S. Majumdar, R. Tewari, G.K. Dey, *Metall. Mater. Trans. A* 44 (2013) 2258–2269.
- [17] Y. Guo, L. Jia, S. Sun, B. Kong, J. Liu, Z. Hu, *Mater. Des.* 109 (2016) 37–46.
- [18] L. Yin, L. Yang, D. Yi, *Mater. Sci. Technol.* 21 (2005) 579–582.
- [19] S. Mathieu, S. Knittel, P. Berthod, S. Mathieu, M. Vilasi, *Corros. Sci.* 60 (2012) 181–192.
- [20] D.P. Moon, *Mater. Sci. Technol.* 5 (1989) 754–764.
- [21] M. Pons, M. Caillet, A. Galerie, *Mater. Chem. Phys.* 15 (1986) 45–60.
- [22] V.A.C. Haanappel, M.F. Stroosnijder, *Surf. Eng.* 15 (1999) 119–125.
- [23] J.M. Hampikian, M. Saqib, D.I. Potter, *Metall. Mater. Trans. B* 27 (1996) 491–500.
- [24] F.J. Pérez, E. Otero, M.P. Hierro, C. Gómez, F. Pedraza, J.L. de Segovia, E. Román, *Surf. Coat. Technol.* 108–109 (1998) 127–131.
- [25] J.F. Ziegler, M.D. Ziegler, J.P. Biersack, *Nucl. Instrum. Methods Phys. Res. B* 268 (2008) 1818–1823.
- [26] M.P. Arbuzov, V.G. Chuprina, *Sov. Phys. J.* 8 (1965) 87–89.
- [27] S.X. Jin, L.P. Guo, Z. Yang, D.J. Fu, C.S. Liu, W. Xiao, R. Tang, F.H. Liu, Y.X. Qiao, *Nucl. Instrum. Methods Phys. Res. B* 269 (2011) 209–215.
- [28] L.M. Wang, S.X. Wang, R.C. Ewing, A. Meldrum, R.C. Birtcher, P.N. Provencio, W.J. Weber, H. Matzke, *Mater. Sci. Eng. A* 286 (2000) 72–80.
- [29] Y. Li, X. Fang, B. Xia, X. Feng, *Scr. Mater.* 103 (2015) 61–64.
- [30] J.V. Landuyt, *Phys. Status Solidi* 6 (1964) 957–974.
- [31] B.V. Mahesh, R.K.S. Raman, *Metall. Mater. Trans. A* 45 (2014) 5799–5822.
- [32] Z.B. Wang, N.R. Tao, W.P. Tong, J. Lu, K. Lu, *Acta Mater.* 51 (2003) 4319–4329.